

On the mechanics of inhaled bronchial transmission of pathogenic microdroplets generated from the upper respiratory tract, with implications for infection onset

Saikat Basu *

Department of Mechanical Engineering, South Dakota State University, Brookings, South Dakota 57007, USA
(Dated: April 29, 2025)

Could the microdroplets formed by viscoelastic fragmentation of mucosal liquids within the upper respiratory tract (URT) explain the brisk onset of deep lung infection following initial URT infections? Generally, particulates, inhaled through the nostrils and therefore navigating the intricate topography of the anterior nasal cavity, can efficiently reach the lower airway only if they are small enough, typically $\lesssim 5 \mu\text{m}$. However, the fate of larger particulates, many exceeding $5\text{-}\mu\text{m}$ in diameter, that are sheared from the initial infection sites along the intra-URT mucosa during inhalation remains unresolved. These particulates originate primarily from the nasopharynx, oropharynx, and the laryngeal chamber containing the vocal folds. To investigate, this study employs a computed tomography-based three-dimensional anatomical airway reconstruction, isolating the tract from the larynx and mapping the tracheal cavity through to the third generation of the tracheobronchial tree; constituent transport across the distal bronchial outlets is also recorded to assess deep lung penetration. Within the defined geometry, airflow simulations are conducted with the Large Eddy Simulation scheme to replicate relaxed inhalation at 15 L/min flow rate. Against the ambient air flux, numerical experiments are performed to monitor the transport of particulates (aerosols/droplets) with diameters $1 - 30 \mu\text{m}$, bearing physical properties akin to aerosolized mucus with embedded virions. The full-scale numerical transmission trends are consistent with findings from our reduced-order mathematical model that conceptualizes the influence of intra-airway vortex instabilities on local particle transport through point vortex idealization in an anatomy-guided two-dimensional potential flow domain. The results collectively demonstrate markedly elevated lower airway penetration by URT-derived particulates, even by those as large as 10 and 15 μm . The high viral load, often exceeding the pathogen-specific infectious dose, carried by such droplets into the bronchial spaces of the sample airway, provides a plausible mechanistic explanation for the accelerated seeding of secondary lung infection.

I. INTRODUCTION

When inhaled air sweeps past the mucociliary coating of the upper respiratory tract (URT), interfacial interactions lead to localized viscoelastic stretching and breakup of mucosal layers resulting in the formation and release of microdroplets [1–3], which could then be pushed downwind by the airflow streamlines. Prominent instability effects when the viscoelastic layer (mucus) resting on a viscous fluid film (serous fluid) is exposed to the incoming airflow are to be noted in this context; e.g., see [4]. The mechanism is analogous to numerous observations from the reverse process: exhalation [5–8]. The expiratory transport regimes, for intense respiratory events [9] and even during silent breathing [10], often involve mucus fragmentation and subsequent emission of liquid particulates spanning a wide range of length scales. From that paradigm, if we pivot our attention to inhaled (i.e., *into* the airway) transport, some immediate questions that come forth concern the fate of the intra-URT particulates generated during inhalation and their probable relevance in progressive disease transmission, especially to the deep lungs. On that note, the present study, through numerical experiments performed in a three-dimensional anatomical airway reconstruction and with simulation-informed reduced-order analytical validation in an anatomy-inspired two-dimensional channel, attempts to answer the following main queries:

- Q_1 . If inhaled from outside and consequently navigating the complex anterior nasal topography, the dominant inertial motion as well as gravitational impaction for particulates larger than $5 \mu\text{m}$ may, in general, prevent their penetration to the lower airway [11, 12]. However, is this also true for particulates of similar sizes shed through mucus separation at the back of the nasal passage from the URT sub-sites like the nasopharynx, oropharynx, and from around the vocal folds during inhalation? Hypothetically, with such particulates still being airborne at the larynx (see Fig 1), the relatively straight structural shape of the downwind tract up to the tracheal base may facilitate their penetration into the lower airway.

* Saikat.Basu@sdstate.edu

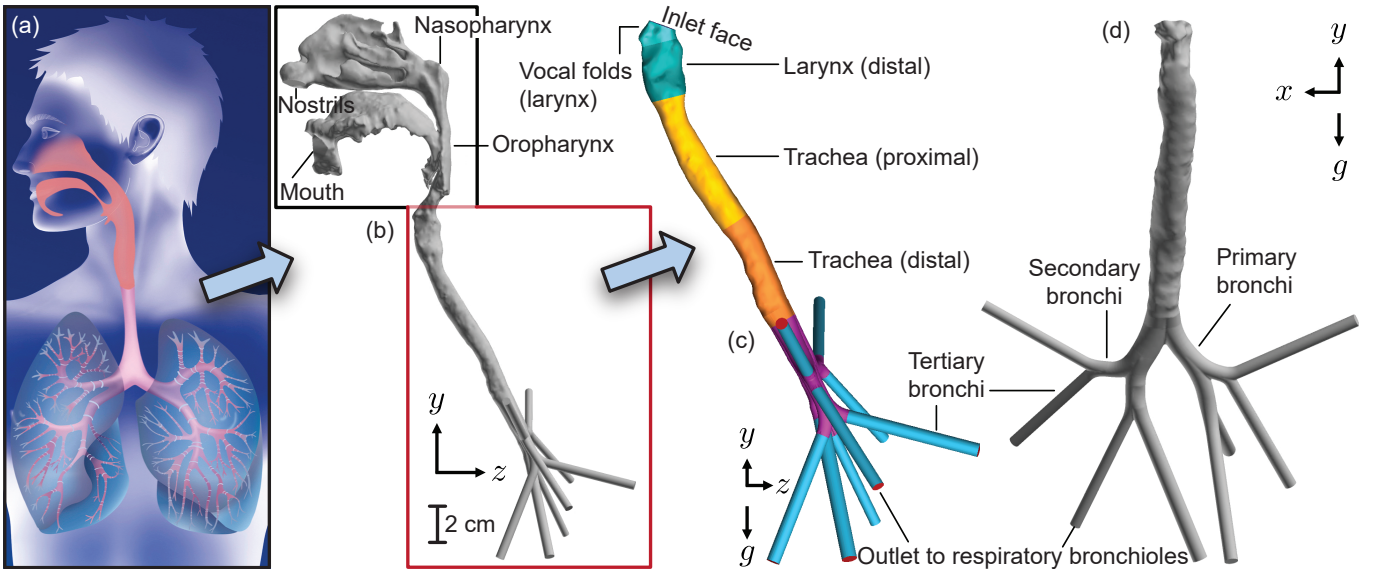


FIG. 1. **Defining the physiological domain.** (a) A demonstrative cartoon of the human respiratory system, encompassing the upper respiratory tract, the mouth, and the lower respiratory tract, extending till the deep lungs. The visual is adopted with a perpetual license agreement from the Getty Images[®]. (b) Sample computed tomography (CT) imaging-based reconstruction of an adult human airway. It serves as a three-dimensional anatomically realistic equivalent of the cartoon in panel (a), with regions included till generation 3 (tertiary bronchi) of the tracheobronchial tree. For confirmation, note that there are 8 distal outlets (see panels (b)-(d)), implying $2^{G_n} = 8$, where $G_n = 3$ is the generation number, considering two-way bifurcation for each bronchial tube at every transition [22]. The domain within the red box is isolated for the numerical experiments on inhaled downwind transport of microdroplets generated from the upper respiratory tract. The isolated region is additionally shown in panel (c) for the sagittal view with anatomical demarcations and in panel (d) for the coronal view. The symbol g signifies the gravity direction in the numerical simulations and the subsequent analytical framework, with x , y , and z defining the spatial orientation of the test cavity. Panel (b) additionally highlights the geometric length scale.

Q_2 . What is the viral load transmitted to the lower airway by particulates originating from the infected intra-URT tissue surfaces? Could this mechanism, in general, explain the rapid onset of lung infection following the initial infection and the emergence of symptoms at URT sub-sites, such as the nasopharynx? First proposed (to the author's knowledge) in [13], the veracity of such a mechanism can dispel the caveat concerning time-scale inconsistencies whereby attributing the rapid downwind progression of infection solely to tissue-level replication of the invading pathogen could be a stretch.

This study addresses Q_1 through full-scale numerical tracking of inhaled constituents inside a representative anatomically accurate airway geometry with a supporting reduced-order anatomy-guided mathematical model of the system. The anatomical test geometry extends up to the third generation of bronchial branching, with cavity outlets leading into finer respiratory bronchioles; see Fig 1. To generate a summative assessment of bronchial deposition alongside deep lung penetration of URT-derived particulates, this study extracts and combines: (a) the simulated bronchial deposition percentages up to generation 3; and (b) the percentage of particulates progressing further downwind through the distal bronchial outlets into the deeper respiratory bronchioles. To note, the term *deep lungs* refers to the lower regions of the respiratory system where gas exchange primarily occurs. This domain includes the bronchioles, alveolar ducts, and alveoli [14]. A detailed analysis of, say, the alveolar deposition trends in the deeper regions of the lungs lies beyond the scope of the present methodology. Using physiological modeling in a test respiratory domain, this paper exclusively assesses the lower airway penetration potential for URT-derived pathogenic microdroplets and how the mechanism could be correlated to secondary infection onset. However, for supplementary reading, comprehensive bronchial deposition profiles for (mostly pharmaceutical) particles administered nasally and/or orally from outside can be found in several excellent studies; e.g., see [15–21].

Next for Q_2 , the fluid dynamics findings on particulate penetration are integrated with virological parameters, such as the sputum viral concentration [23] for a representative pathogen (SARS-CoV-2), and the projected viral load transmitted to the bronchial pathways is compared against the verified infectious dose of the pathogen [24, 25]. The resulting translational analysis helps assess the proclivity for lower airway infection that is driven by inhalation of aerosolized intra-URT mucosal remnants. It is worth noting that this *in silico* approach, rooted in the underlying respiratory flow physics as discussed here, is agnostic to any virus specificity and potentially extensible to other

respiratory pathogens by integrating the fluid mechanics outcomes of inhaled transport with appropriate virological and immunological data. In that context, this work can contribute toward advancing an emerging niche sub-field that brings together classical fluid dynamics and virology [25–30]. For select recent relevant studies on deep lung kinetics and pathophysiology, the reader may refer to [13, 31–34]; additionally, one may peruse [35, 36] for engaging accounts of airway flow physics, its potential impact on lung function, and the pertinent open problems.

II. MATERIALS AND METHODS

Numerical modeling of inhaled downwind transport of URT-derived microdroplets

As is the case for inhaled transport of microdroplets (also referred to as particulates, or equivalently simply at times as particles in this exposition) through the respiratory cavity, in numerical simulations involving the dispersion of small particles under dilute conditions—the common approach assumes one-way coupling. This reduction implies that while the airflow continuum carries the particulates, the impact of such particulates on the underlying flow regimes could be disregarded. Consequently, the ambient airflow field is initially resolved, and the flow outcomes are subsequently employed to numerically solve the relevant particle equations of motion.

In this study, we have used Large Eddy Simulation (LES) scheme with dynamic subgrid-scale kinetic energy transport model to numerically replicate the inhaled air flux through an anatomically realistic airway reconstruction. To model the inhaled particle transport therein, we have applied the Lagrangian approach which is more suitable (compared to the Eulerian methods) for the dilute suspension of relatively large particles for which inertia could often be dominant in determining the spatial trajectories and eventual deposition spots. The simulated airflow field is coupled with the Lagrangian particle transport analysis to derive the intra-airway deposition and penetration trends.

1. Anatomical geometry reconstruction, spatial discretization, and mesh sensitivity analysis

From de-identified, high-resolution, medical-grade computed tomography (CT) imaging, this study has first reconstructed a complete three-dimensional adult respiratory airway [37]; see Fig 1a-b. The extraction warranted a radio-density thresholding between -1024 to -300 Hounsfield units [38, 39] to capture the airspace from the CT slices. Aiming to address Q_1 and Q_2 (pitched in the introduction), the reconstruction has then been digitally redacted to focus on the space mapping the vocal fold region of the larynx (space with highest concentration of liquid particulates formed from intra-URT mucosal fragmentation) along with the distal laryngeal chamber, the trachea, and the lower airway extending till generation 3 of the tracheobronchial tree, incorporating the primary, secondary, and tertiary bronchi, followed by the respiratory bronchiolar outlets as entry to the deeper recesses of the lungs. See Fig 1c-d for the redacted test geometry with the described regions marked out. To prepare the domain for numerical simulations, a grid refinement analysis was conducted with the test cavity being spatially segregated into 0.5, 1.0, 1.5, 2.0, 2.5, and 3.0 million graded, unstructured, tetrahedral elements, along with four layers of pentahedral cells (with 0.025-mm height for each cell and an aspect ratio of 1.1) extruded at the airway cavity walls [40] to resolve the near-wall particulate dynamics; see Fig 2a-h. The variables assessed in the sensitivity study included the resistance \mathcal{R} (in Pa.min/L) to the simulated inhaled airflow, calculated as $|\Delta P|/Q$, where $|\Delta P|$ in Pa represents the inlet-to-outlet pressure gradient driving the flow and Q denotes the volumetric flux in L/min; the area-weighted average airflow velocity magnitude V_o (in m/s) at the outlet surfaces of the geometry; and the transmission efficiency η (in %) within the bronchial pathways for representative particulate sizes of 1, 5, 10, and 20 μm . The deposition and penetration efficiency η quantifies the cumulative bronchial transmission trend for each particulate size—summing the deposition rates at the primary, secondary, and tertiary bronchi, together with the penetration rate through the distal bronchiolar outlets into the deeper lung regions (see Fig 1c-d). The fluctuation trends of the tracked variables are shown in Fig 2i-k. Specifically, the simulation results yield:

$$\begin{aligned} \sigma(\mathcal{R})_{\text{All}} &= 0.0051 \text{ Pa.min/L}, & \sigma(\mathcal{R})_3 &= 0.0041 \text{ Pa.min/L}, \\ \sigma(V_o)_{\text{All}} &= 0.0085 \text{ m/s}, & \sigma(V_o)_3 &= 0.0026 \text{ m/s}, \\ \sigma(\eta)_{\text{All}} &= 7.94\%, & \sigma(\eta)_3 &= 0.44\%, \end{aligned} \tag{1}$$

where $\sigma(\cdot)_{\text{All}}$ denotes the standard deviation across all six grids and $\sigma(\cdot)_3$ denotes the standard deviation of the simulated data from the last 3 grids (i.e., cases with 2.0, 2.5, and 3.0 million unstructured tetrahedral cells). Based on the asymptotic convergence trend observed in these final three cases, the intermediate 2.5-million cell grid resolution was selected for the overall study. The choice is consistent with detailed studies on grid convergence and computational

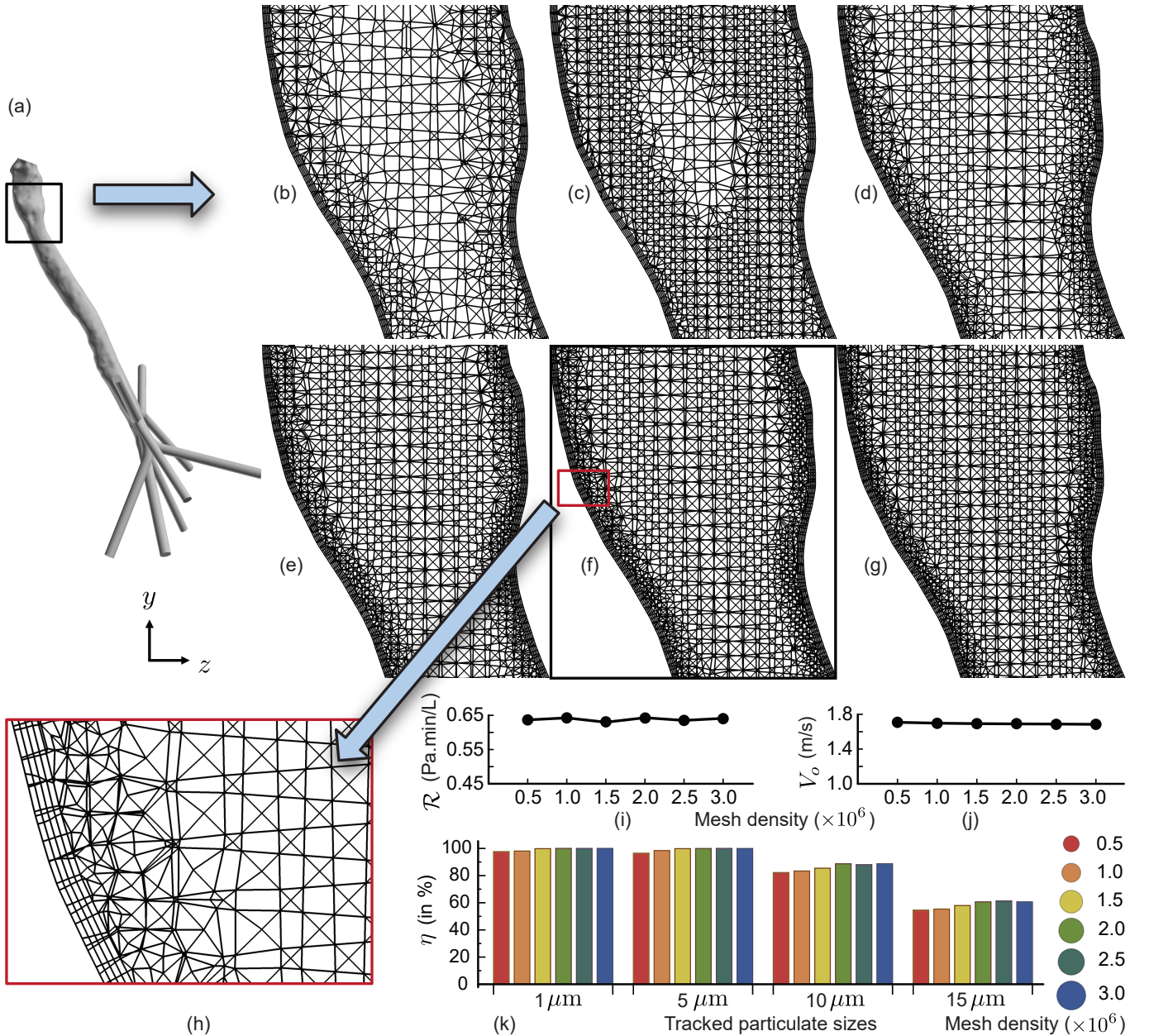


FIG. 2. **Assessing the numerical sensitivity.** Panel (a) marks the location of the demonstrated unstructured tetrahedral meshes spatially refined with the following cell counts (in million): (b) 0.5, (c) 1.0, (d) 1.5, (e) 2.0, (f) 2.5, (g) 3.0. Panel (h) highlights the four layers of pentahedral cells used for near-wall refinement. Panels (i)-(k) present the computed flow and particulate transport variables across the six mesh resolutions: (i) resistance \mathcal{R} to inhaled airflow, (j) area-weighted average airflow velocity V_o at the outlet faces, and (k) deposition (or, penetration) rate η (%) in bronchial pathways for select particle sizes of 1, 5, 10, and 20 μm . The circle sizes to the right of panel (k) represent the number of tracked particulates in each simulation, scaled proportionally: red = 597, orange = 831, ocher = 1208, green = 1459, dark green = 1622, and blue = 1954 tracked particulates per size. Tracked particle counts equal the number of surface elements at inlet, directly proportional to the spatial resolution of the respective mesh.

stability for simulating physiologically realistic airflow and particle deposition in the human respiratory system; e.g., see [41].

Notably, while using the LES scheme, a finer mesh refinement typically leads to more precise outcomes. For instance, at the upper limit, achieving results akin to Direct Numerical Simulation (DNS) is possible if the grid dimensions are

smaller than the Kolmogorov scale, \mathcal{K} , defined as [42]:

$$\mathcal{K} = \left(\frac{\nu^3}{\varepsilon} \right)^{1/4}, \quad (2)$$

with ε as the turbulence dissipation rate and ν being the fluid kinematic viscosity. Another length scale of note is the Taylor scale, λ , which typically exceeds \mathcal{K} and is defined as:

$$\lambda = \left(\frac{10\nu k}{\varepsilon} \right)^{1/2}, \quad (3)$$

with k being the turbulence kinetic energy. From the simulation data of the inhaled airflow field, it is seen that both λ and \mathcal{K} collapse to $\mathcal{O}(10^{-4})$ m, while the mean grid scale is also $\rightarrow \mathcal{O}(10^{-4})$ m, suggesting that the test grid has been sufficiently resolved for reliable estimation of the transport parameters.

2. Numerical simulation of inhaled airflow

We have implemented the LES approach to numerically model the inhaled airflow, with eddies exceeding the grid scale explicitly resolved, whereas those that are smaller than the grid scale are approximated. Specifically, fluctuations below the grid size, referred to as subgrid scales, are filtered out, and their impact on larger scales is replicated through modeling. Assuming incompressible, isothermal conditions for the inhaled air flux, the filtered continuity and Navier–Stokes equations are respectively:

$$\frac{\partial}{\partial x_i} (\rho \bar{u}_i) = 0 \quad (4)$$

and

$$\frac{\partial \bar{u}_i}{\partial t} + \frac{\partial}{\partial x_j} (\bar{u}_i \bar{u}_j) = -\frac{1}{\rho} \frac{\partial \bar{p}}{\partial x_i} + \frac{\partial}{\partial x_j} \left(\nu \frac{\partial \bar{u}_i}{\partial x_j} \right) - \frac{\partial \tau_{ij}}{\partial x_j}. \quad (5)$$

Here \bar{u}_i represents the filtered (i.e., resolved) velocity, \bar{p} is the filtered pressure, ν and ρ are respectively the kinematic viscosity and the density of inhaled warmed-up air, and τ_{ij} is the subgrid scale (SGS) stress tensor defined by

$$\tau_{ij} - \frac{1}{3} \tau_{kk} \delta_{ij} = -\nu_{sgs} \left(\frac{\partial \bar{u}_i}{\partial x_j} + \frac{\partial \bar{u}_j}{\partial x_i} \right), \quad (6)$$

where ν_{sgs} is the SGS kinematic viscosity and δ_{ij} is the Kronecker delta. It is to be noted that τ_{kk} , which comprises the isotropic part of the SGS stresses, is not modeled but added to the filtered static pressure. Subsequently, the instantaneous field velocity is given by

$$u_i = \bar{u}_i + u_i^{sgs}, \quad (7)$$

with u_i^{sgs} representing the SGS velocity fluctuations. The flow patterns and particle dispersion within the human respiratory system will be strongly impacted by the secondary flows common in such complex geometries and by the airflow transitions between laminar and turbulent regimes. To simultaneously capture the transitional features as well as the secondary flow formations, this study uses the dynamic subgrid-scale kinetic energy transport model [43–45]. Therein the SGS kinematic viscosity, ν_{sgs} , is obtained from the Kolmogorov-Prandtl hypothesis [46] in the following form:

$$\nu_{sgs} = C_k k_{sgs}^{1/2} \Delta_f. \quad (8)$$

In the above equation, C_k is a constant value and Δ_f is the filter size computed as $\Delta_f \equiv (\text{grid cell volume})^{1/3}$. The term k_{sgs} represents the SGS kinetic energy, defined by

$$k_{sgs} = \frac{1}{2} (\bar{u}_i \bar{u}_j - \bar{u}_i \bar{u}_j). \quad (9)$$

To derive k_{sgs} , we solve the following filtered transport equation:

$$\frac{\partial k_{sgs}}{\partial t} + \frac{\partial}{\partial x_j} (k_{sgs} \bar{u}_j) = \frac{\partial}{\partial x_j} \left(\nu_{sgs} \frac{\partial k_{sgs}}{\partial x_j} \right) + \frac{\partial \bar{u}_i}{\partial x_j} \left[\nu_{sgs} \left(\frac{\partial \bar{u}_i}{\partial x_j} + \frac{\partial \bar{u}_j}{\partial x_i} \right) - \frac{2}{3} k_{sgs} \delta_{ij} \right] - C_\varepsilon \frac{k_{sgs}^{3/2}}{\Delta_f}, \quad (10)$$

with the model constants in the previous equations, i.e., C_k and C_ε , being determined dynamically [43].

Applying the LES scheme as described above, the inhaled airflow through the anatomical airspace was replicated for 15 L/min inhalation rate, conforming with normal relaxed breathing conditions [47]. See Fig 1c for the pressure inlet face at the location of vocal folds in the larynx and for the pressure outlets at the distal ends of the reconstructed generation 3 bronchial tubes. Enforcing no slip (i.e., zero velocity) boundary condition at the airway walls, the pressure gradient-driven simulation used time-steps of 0.0002 s. The latter was chosen based on reported findings [45] on the time-step size warranted to fully resolve the unsteady turbulent airflow field in a realistic upper airway model, it being smaller than the Kolmogorov time scale $= (\nu/\varepsilon)^{1/2}$ [42], for a flow solution time of 0.35 s. The simulation was executed on a segregated solver with pressure-velocity coupling and second-order upwind spatial discretization. For the transient formulation, a bounded second-order implicit scheme was employed, to strike a balance between accuracy (due to the second-order formulation), stability (from the implicit approach), and boundedness (to prevent non-physical oscillations). The eventual solution convergence was monitored by minimizing the mass continuity residual to $\mathcal{O}(10^{-3})$ and the velocity component residuals to $\mathcal{O}(10^{-6})$. Also, considering the warmed-up state of inhaled air passing through the respiratory pathway, the air density ρ was set at 1.204 kg/m³ in the simulations, with 15.16×10^{-6} m²/s as its kinematic viscosity ν .

3. Numerical experiments for particulate transport

Against the solved airflow field, the particulates formed intra-URT were tracked from the vocal fold region of the larynx (see the marked inlet face in Fig 1c). The air-particle phases were one-way coupled with the particles (assumed spherical) being impacted by the ambient flow field; the underlying flow domain was considered quasi-steady while evaluating the particle transport parameters. Lagrangian-based inert discrete phase model, with a Runge-Kutta solver, was used to numerically integrate the particle transport equation:

$$\frac{du_{pi}}{dt} = \frac{18\mu}{d^2\rho_p} \frac{C_D Re_p}{24} (u_i - u_{pi}) + g_i \left(1 - \frac{\rho}{\rho_p}\right) + F_i. \quad (11)$$

Here u_{pi} represents the particulate velocity, ρ_p is the material density of the particulates, d represents the particulate diameter, Re_p is the particulate Reynolds number, g_i signifies the gravitational acceleration in the i direction, C_D is the drag coefficient, and F_i represents additional body forces per unit particulate mass in the form of the Saffman lift force exerted by a typical flow-shear field on small particulates transverse to the airflow direction. In this context, note that the solution scheme considered the particulates to be large enough to ignore any Brownian motion effects on their dynamics.

To evaluate the drag component in equation 11, the quantities Re_p and C_D are respectively computed as: $Re_p = \rho_p d |u_i - u_{pi}| / \mu$ and $C_D = a_1 + a_2/Re_p + a_3/Re_p^2$; where μ is the molecular viscosity of the ambient fluid (i.e., air), while a_1 , a_2 , and a_3 are functions of Re_p determined based on the spherical drag law [48]. Subsequently, the particulate trajectories are derived from their spatiotemporal locations, $x_i(t)$, obtained by numerical integration of the following velocity vector equation:

$$u_{pi} = \frac{dx_i}{dt}. \quad (12)$$

Intra-airway aerial tracking of a particulate pathline was stopped once it entered the mesh element layer adjacent to the enclosing walls of the respiratory cavity. The particulates escaping through the bronchiolar outlets were also recorded, and represented the particulates penetrating to the respiratory bronchioles and deep lungs. The numerical experiments in this study tested particulates of diameters 1 – 30 μm (with increments of 1 μm). In total, $\mathcal{N} = 1622$ particulates of each size were tracked; \mathcal{N} being the number of surface elements in the mesh layer mapping the inlet face (see Fig 1). Also, considering that saliva-mixed mucus is 99.5% water [49], the material density of the particulates was assumed to be $\rho_p = 1.00175$ g/ml, approximated as the weighted average (see equation 13 below) between 99.5% water and the residual pathogenic and biological non-volatile compounds with a representative density of $\rho_{nv} = 1.35$ g/ml; e.g., for protein [50], the density being independent of the nature of the protein and particularly independent of its molecular weight. The weighted average calculation for the simulated particulate density is as follows:

$$\rho_p = \frac{0.5 \times \rho_{nv} + 99.5 \times \rho_w}{100}, \quad (13)$$

with $\rho_w = 1.0$ g/ml representing the density of water. The consideration of inertness for the tracked particulates (per equation 11) also implies that the modeling framework was agnostic to the biological nuances of the embedded constituents in the particulates, beyond the imposition of the appropriate physical properties, e.g., density. The modeling approach also discounted any heat transfer effects between the flow constituents and the surrounding tissues enclosing the anatomical airspace.

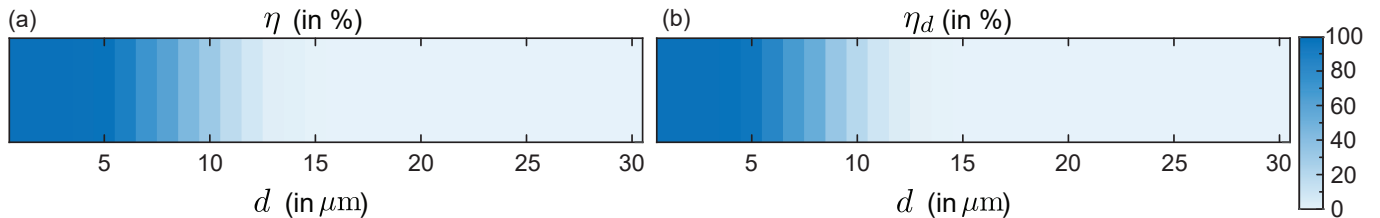


FIG. 3. **Transmission trend for particulates inhaled from outside and navigating the complete anterior airway.** (a) η represents the cumulative deposition percentages at the primary, secondary, and tertiary bronchi, together with the penetration rate through the bronchiolar outlets into the deeper lung regions; (b) η_d isolates the penetration rate through the bronchiolar outlets with the tracked particulates moving into the deeper lung regions. The reader may find it insightful to compare the trend reported here with Fig 6a-b on the navigation trend for particulates generated within the URT (and still airborne at the larynx). In the latter scenario, the larger particulates exhibit much greater efficiency at penetrating to the lower airway.

4. Supplementary ‘diversion’: bronchial transmission trend for particulates inhaled from outside

While the focus of this study is singularly on the downwind bronchial transmission of particulates generated within the URT, it would be of scholarly interest to undertake a brief detour at this point to explore an auxiliary question (that has been nonetheless well-explored in literature): for the particulates inhaled from the external environment, which particulate sizes would be efficient at penetrating to the bronchial spaces? Here, we address this question specifically for the test geometry used in this study, through transport simulations within its non-redacted complete anatomy (Fig 1b) wherein inhaled particulates are entering the airway through both the left and right nostrils.

Comparing the cavity spaces in the complete airway geometry (Fig 1b) and the redacted model (Fig 1c-d), the volume of the former is approximately 3.48 times larger than that of the redacted system. Accordingly, following the described meshing protocol, the full airway was discretized into $2.5 \text{ million} \times 3.48 = 8.7 \text{ million}$ unstructured tetrahedral elements, with four layers of pentahedral cells lining the cavity surfaces. Using this meshed geometry, particulate transport was simulated at an inhaled airflow rate of 15 L/min, following methods outlined earlier. The only modification was setting the material density of the inhaled particulates to 1.3 g/ml, consistent with typical values for environmentally dehydrated respiratory ejecta [25, 49], which constitutionally form the pathogen-bearing particulates inhaled from external air.

Fig 3 demonstrates the bronchial transmission trend for particulates inhaled from outside. Therein, panel (a) shows the cumulative transmission percentage, η , at the primary, secondary, and tertiary bronchi, together with the penetration rate (in %) through the geometry outlets that serve as entry to the respiratory bronchioles. Panel (b) solely presents η_d , the penetration rate through the bronchiolar outlets, indicating the proportion of inhaled particulates reaching the deeper lung regions. Considering select particulate sizes, η starts at 99.36% for particulates of diameter $d = 1 \mu\text{m}$, decreases to 96.86% for $d = 5 \mu\text{m}$, to 31.46% for $d = 10 \mu\text{m}$, and approaches 0% for $d = 15 \mu\text{m}$ and larger. Remarkably though, as we will find later (in the results), for particulates generated *within* the URT, the quantity η shoots up significantly, approaching 90% for $d = 10 \mu\text{m}$ and steadily sustaining at $> 60\%$ even for $d = 15 \mu\text{m}$.

A. A simplified analytical model for inhaled transport through the laryngotracheal space

To verify the particulate transport trends to the bronchial domain as derived numerically, let us invoke a simulation-informed reduced-order analytical model (S-ROAM), with a two-dimensional channel mimicking the laryngotracheal domain. Therein, the inhaled airflow is modeled in the dimensionless complex χ plane, with $\chi = \alpha + i\beta$ and $i\beta$ aligned with the channel’s streamwise axis; see Fig 4. The two-dimensional channel has its streamwise length and cross-stream width based on the averaged dimensions of the anatomical tract from Fig 4a-b. The channel walls are placed at $\alpha = 0, 1$. Based on the geometric inputs, the S-ROAM enforces $L/W \approx 9$, where L represents the streamwise channel length and W is the inlet width. For a detailed exposition of this classical modeling approach for complex respiratory systems, see our recent preprint [51].

The reduced system modeled the core of an extended vortex patch emerging in the full-scale numerical simulation as a random collection of five point vortices distributed over the area of the simulated vortex core (on the channel plane, mapping the mid-sagittal section of the three-dimensional cavity; see Fig 4b), bearing dimensionless circulations $\Gamma_i = \omega A/5UW$, where ω was the mean vorticity (as determined from the numerical simulations) spread over the patch area A and U is the characteristic streamwise air speed through the channel. From the simulated data, we had: $\omega \approx 1750 \text{ s}^{-1}$, $A \approx 2.65 \times 10^{-5} \text{ m}^2$, and $U = Q/a = 2.16 \text{ m/s}$, with $a = 115.82 \text{ mm}^2$ being the area of the

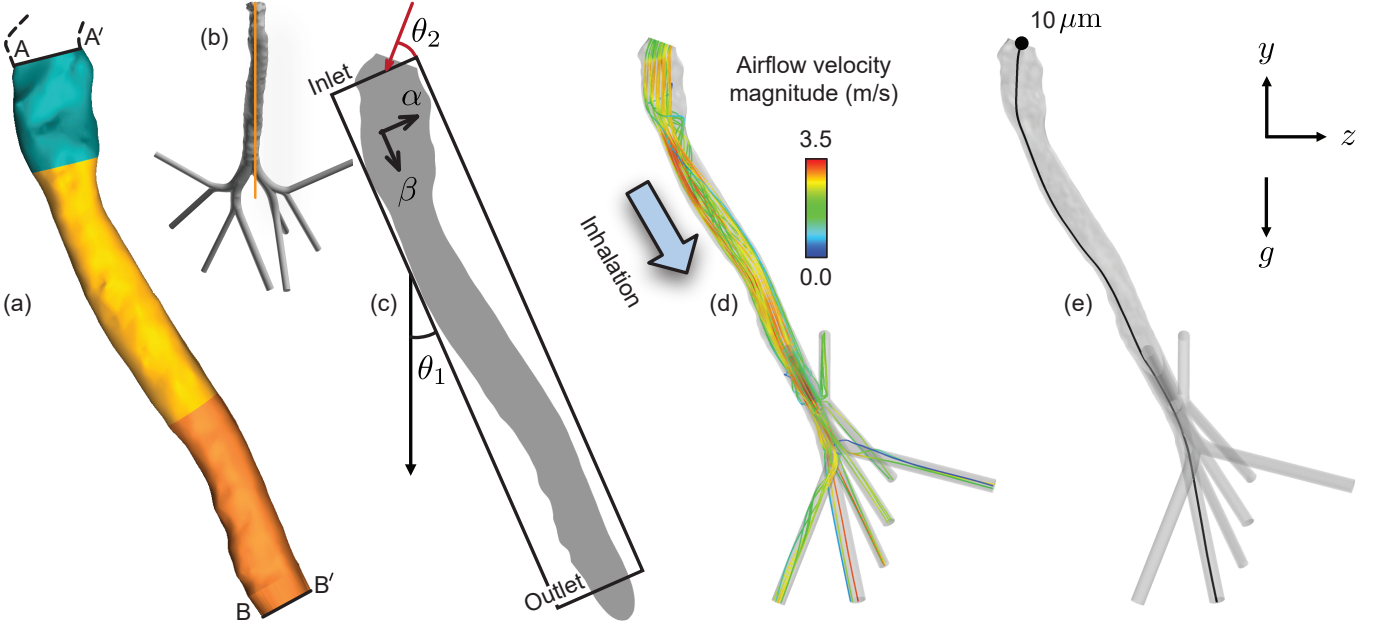


FIG. 4. **Defining the analytical domain, with representative numerical visuals.** (a) Laryngotracheal region upwind from the primary bronchi used to develop a simulation-informed reduced-order analytical model (S-ROAM) for bronchial transmission. AA' marks the larynx upwind face and BB' marks the downwind face of the distal tracheal cavity; see labels in Fig. 1d. The cross-sectional areas of the cavity at AA' and BB' are 108.61 mm^2 and 123.03 mm^2 , respectively. The corresponding hydraulic diameters are 11.03 mm and 12.20 mm , respectively. The linear spatial distance between the two faces is approximately 115.84 mm , at angle $\theta_1 = 23.77^\circ$ to the vertical (direction of gravity in the numerical simulations). Panel (b) highlights the location and orientation of the planar cross-section shown in panel (c) and also previously as the location of the mesh visuals in Fig 2. The vortex strengths and positions for the S-ROAM are extracted from the simulated data mapping this two-dimensional plane; the plane cuts through the entire cavity of panel (a). $\theta_2 = 33.94^\circ$ is the assumed angle in S-ROAM, at which microdroplets enter the AA' inlet face and is governed by the anatomical shape of the cavity upwind from AA' (marked by the dashed black traces; also see Fig 1). (d) 30 randomly selected representative velocity streamlines extracted from the numerically simulated inhaled airflow field. (e) Simulated trajectory of a representative $10\text{-}\mu\text{m}$ particulate. The geometric centroid of the inlet face, marked by the solid circle, was chosen as the particulate's position at tracking time $t = 0$.

inlet face and $Q = 15 \text{ L/min} = 0.00025 \text{ m}^3/\text{s}$ being the simulated inhalation flux. Based on the angular orientation of the modeled core in the simulated vorticity field, the model point vortices were placed on a line that subtended $\approx 2.2^\circ$ in counter-clockwise sense with the vertically downward direction. The anatomical planar section from which the vorticity information was extracted is shown in Fig 4c.

In the S-ROAM, the straight streamlines at the channel walls were established through inclusion of periodic images of the point vortices in the cross-stream α direction. The resulting (dimensionless) complex potential for this system, with a dimensionless background speed of unity, is [52–54]:

$$F(\chi) = \phi(\alpha, \beta) + i\psi(\alpha, \beta) = i\chi + \sum_{i=1}^5 \frac{\Gamma_i}{2\pi i} \log \left\{ \frac{\sin[\pi(\chi - \chi_i)/2]}{\sin[\pi(\chi + \chi_i^*)/2]} \right\}, \quad (14)$$

with ϕ as the velocity potential and ψ as the real-valued flow streamfunction; the asterisk denotes complex conjugation. Subsequently, the inhaled particulate motion was analytically derived using a simplified version of the Maxey-Riley equation [55, 56], in the two-dimensional vector form [57, 58]:

$$\frac{d\mathbf{w}}{dt} = - \left[\mathbf{J} + \frac{2St^{-1}}{3(\sigma+1)} \mathbf{I} \right] \cdot \mathbf{w} + \frac{\sigma}{\sigma+1} \left(Fr^{-2} \mathbf{g} - \frac{D\mathbf{u}}{Dt} \right). \quad (15)$$

Here \mathbf{u} is the local fluid velocity in vector coordinates, $\mathbf{w} = \mathbf{u}_p - \mathbf{u}$ is the relative velocity of a particulate with velocity \mathbf{u}_p , \mathbf{J} is the two-dimensional Jacobian matrix, \mathbf{I} is the identity matrix, \mathbf{g} implies gravity, with the nondimensional parameters being Stokes number $St \equiv d^2U/18\nu L$, Froude number $Fr \equiv U/\sqrt{gL}$, and $\sigma \equiv 2(\rho_p - \rho)/3\rho$.

Although viscous effects are neglected in the above velocity model, particle drag is included. This form of the model ignores the Faxen correction terms and the Basset-Boussinesq history force. Particulates are assumed to be

entering the S-ROAM domain (inclined at an angle $\theta_1 = 23.77^\circ$ to the direction of gravity, per the general shape and orientation of the test anatomical cavity) with speed U and at an angle of $\theta_2 = 33.94^\circ$ with respect to the S-ROAM's α -axis, mimicking the simulated motion of particles entering the region; see Fig 4c. As representative examples, particulate trajectories were derived for two initial positions at the mid-point and near the right edge of the reduced channel's inlet span, and for seven different particulate diameters, namely 5, 10, 15, 20, 25, 30, and (as an extremal case) 50 μm .

B. Connecting the fluid dynamics outcomes to pathogen-specific virological data

From the numerical experiments, this study has deduced the simulated deposition and penetration efficiencies of the URT-derived particulates along the bronchial tubes (see Table I) and evaluated the respective volumetric transmission to the bronchi. The projected net deposited (at the primary, secondary, and tertiary bronchi) and penetrated (moving into the respiratory bronchioles) volumes are then multiplied with the sputum viral concentration for a specific pathogen (in this study, SARS-CoV-2) to evaluate and compare the viral load transported via inhaled aerial advection of URT particulates to the lower airway and deep lungs, for select test particulate sizes, namely, 1, 5, 10, and 15 μm .

Note that the average sputum viral concentration for SARS-CoV-2 has been reported as $\mathcal{V} = 7.0 \times 10^6$ virions/ml, through count measurements of the RNA copies for the single-stranded virus present in the airway liquid samples collected from hospitalized COVID-19 patients; see [23].

III. RESULTS

A. Bronchial deposition and lower airway penetration as projected from numerical modeling

Fig 4d presents sample inhaled airflow velocity streamlines from the numerical simulation of inhaled airflow. The simulated flux of 15 L/min warranted an inlet-to-outlet pressure gradient of -9.5 Pa. Against the flow field, the test particulates were tracked with their starting locations uniformly distributed on the cross-sectional space spanning the vocal fold region of the laryngeal cavity (commensurate with their hypothesized formation sites at the URT—through breakup of mucus strata along the nasopharynx, the oropharynx, and the vocal folds). A representative particulate trajectory for $d = 10 \mu\text{m}$ has been additionally shown in Fig 4e. At tracking time $t = 0$, the particulate was assumed to be positioned at the geometric centroid of the inlet face. Eventually, the sample particulate penetrates through the outlet to respiratory bronchioles, thereby moving into the deeper lung recesses.

Fig 5a-c and Table I detail the lower airway deposition and penetration data for the tested particulates bearing diameters 1 – 30 μm (with increments of 1 μm). While it is expected that the particulates $\lesssim 5 \mu\text{m}$ would comfortably penetrate to the deeper regions of lungs (as is clearly the case per Table I; see the top rows), the high transmission percentages, e.g., for even the 10- and 15- μm particulates is striking—they being 88.04% and 61.34%, respectively.

B. Viral load transmitted to the lower airway

Table II lists the viral load transmitted to the bronchial pathways, for the representative test particulate sizes 1, 5, 10, and 15 μm . For the time scale T (in days) over which the viral load transmission is to be estimated, we have used 3 days based on reported data [59] on the typical time interval that has revealed confirmed infection onset in the deep lungs subsequent to the emergence of initial symptoms along the URT. Further, applying $\delta t = 5$ s as the average duration for a complete breathing cycle [60], the viral load, L_v , transmitted downwind can be computed as:

$$L_v = \frac{144 \pi d^3 \eta T \mathcal{V} \mathcal{P}(d_i)}{\delta t} \times 10^{-12}. \quad (16)$$

where $\mathcal{P}(d_i)$ is the particle size density function that quantifies the number of microdroplets of size d_i generated during each inhalation cycle. For simplicity, the data in Table II enforced $\mathcal{P} = 1$, irrespective of the particulate size, i.e., the particulate formation rate was conservatively assumed to be 1 per breathing cycle, for each test particulate size. Also, while the reported numbers in Table II are based on the estimates guided by equation 16, the zero viral load assessment for the 1- μm particulates implies that the corresponding transmission estimate from equation 16 resulted in a fractional number $\ll 1$, and bears no physical significance. To note here additionally, for the assumed \mathcal{P} , the quantity L_v exceeded 300 for $d \in [13, 22] \mu\text{m}$. See the conclusion section later for the related translational relevance in infection mechanics.

TABLE I. **Numerical transmission trend:** The numerically simulated bronchial deposition and penetration data are detailed herein. The particulate sizes, that have been explored further in Table II (to formalize the viral transmission trends as a function of the microdroplet dimensions), are in bold font. *Symbols:* d = tested aerosol (or, droplet) diameter; \mathcal{N} = total number of aerosols (or, droplets) tracked for each particulate diameter; n_p = number of deposited particulates in the primary and secondary bronchi; n_t = number of deposited particulates in the tertiary bronchi; n_d = number of particulates penetrating into the respiratory bronchioles toward the deep lungs; η = cumulative deposition (or, penetration) rate (in %) to the bronchial pathways and computed as $100 \times (\sum_j n_j) / \mathcal{N}$, with $j \in \{p, t, d\}$.

Separated particulate size (d , in μm)	\mathcal{N}	n_p	n_t	n_d	Bronchial transmission (η , in %)
1	1622	6	0	1616	100.00
2	1622	33	3	1586	100.00
3	1622	11	0	1611	100.00
4	1622	14	1	1607	100.00
5	1622	33	3	1586	100.00
6	1622	53	10	1559	100.00
7	1622	91	34	1493	99.75
8	1622	136	34	1422	98.15
9	1622	168	51	1277	92.23
10	1622	214	39	1175	88.04
11	1622	229	55	1083	84.28
12	1622	300	56	930	79.28
13	1622	368	59	787	74.85
14	1622	424	60	634	68.93
15	1622	449	93	453	61.34
16	1622	445	90	321	52.77
17	1622	433	111	217	46.92
18	1622	395	108	146	40.01
19	1622	361	104	72	33.11
20	1622	309	86	45	27.13
21	1622	268	63	25	21.95
22	1622	218	49	13	17.26
23	1622	168	22	10	12.33
24	1622	118	4	1	7.58
25	1622	83	0	0	5.12
26	1622	58	0	0	3.58
27	1622	38	0	0	2.34
28	1622	19	0	0	1.17
29	1622	3	0	0	0.18
30	1622	0	0	0	0.00

C. Heaviside trend governing bronchial deposition and penetration

Collapsing the transmission efficiencies from Table I and Fig. 5a on a 2D plane with particulate diameters d (in μm) along the horizontal axis reveals an S-trend with (as expected) a high bronchial penetration for smaller particulate sizes, followed by a gently sloped dip; see Fig 5c. The behavior could be approximated with a modified Heaviside function [61] of the following empirical form:

$$\eta(d) = \mathcal{C}_1 + e^{\mathcal{C}_2 / [1 + e^{k(d + \mathcal{C}_3)}]}, \quad (17)$$

where k and \mathcal{C}_i , with $i \in \{1, 2, 3\}$, are constant fitting parameters. The adopted multivariate Heaviside formalism is particularly suitable for modeling the inverted S-shaped trend of bronchial deposition and penetration as a function of the particulate sizes, owing to its ability to represent sharp yet smooth transitions between high and low deposition rates across different size thresholds. This function effectively captures the nonlinear behavior implicit to respiratory systems, where smaller particulates penetrate deeply into the bronchial pathways, while larger ones tend to deposit more proximally or are filtered out. The mathematical *ansatz* allows for adjustable steepness and transition points, rendering it flexible enough to fit the specific inflection points associated with particle size changes. Herein, the solid red curve, fitting through the numerical data-points, was derived using the Nelder-Mead simplex algorithm for systematic error minimization [62, 63]. The algorithm, also known as the downhill simplex method, is an iterative, heuristic

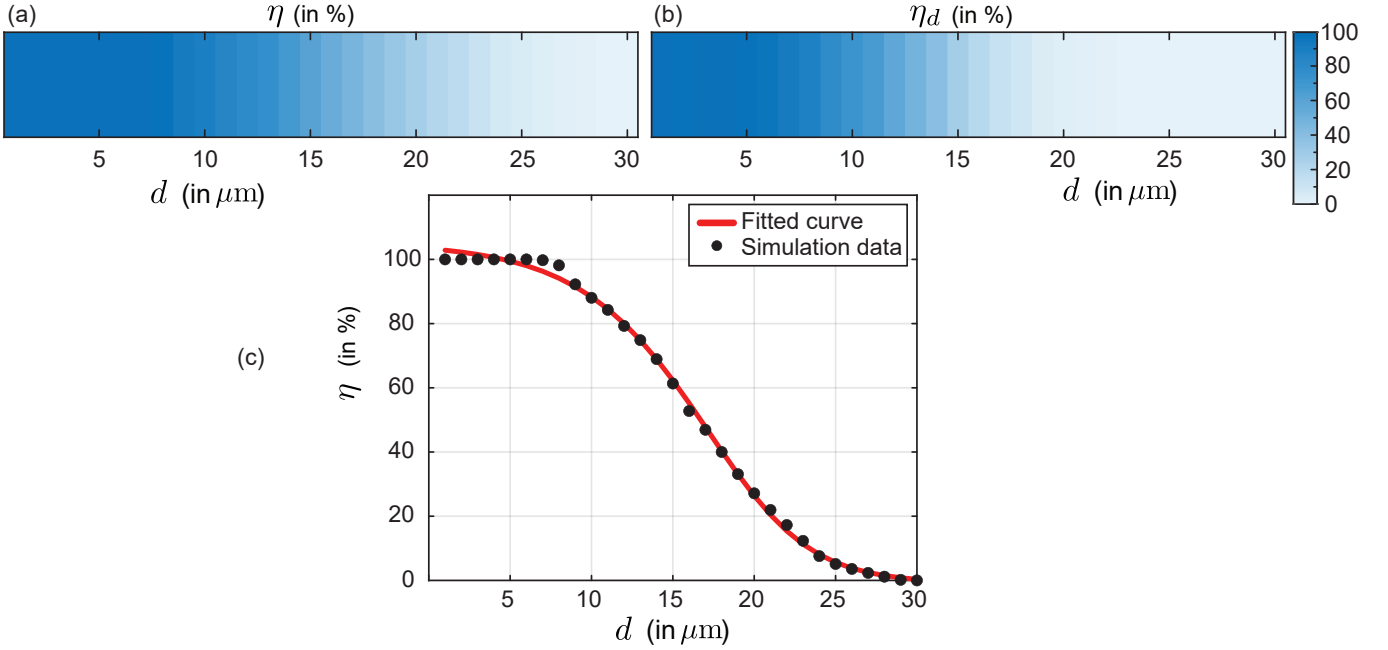


FIG. 5. Numerically simulated transmission trend for URT-derived particulates navigating through the redacted test geometry. (a) η represents the cumulative deposition percentages at the primary, secondary, and tertiary bronchi, as well as the penetration rate through the bronchiolar outlets into the deeper lung regions; (b) η_d isolates the penetration rate through the bronchiolar outlets; (c) The solid red line is a fitted curve of the Heaviside step function form (see equation 17), with the solid black circles showing simulation-derived η values (reported in Table I).

optimization technique designed for unconstrained optimization problems, especially where derivative information is not available or the function is noisy or discontinuous. The curve in Fig 5c invokes the following fitting parameter values:

$$C_1 = -2.1706, \quad C_2 = 4.6755, \quad C_3 = -23.9592, \quad k = 0.23468. \quad (18)$$

D. Analytical projections for particulate transport: consistent with the full-scale numerical findings

Fig 6a demonstrates the vorticity field mapped over the section shown in Fig 4c. In the reduced-order analytical setup, the vortex patch core marked by \mathbb{V} is modeled with a spatial assembly of five point vortices, as described in the methods. In Fig 6b-h, the grey curves show the streamlines of the background flow field in the S-ROAM, with the red curves tracing the sample particulate trajectories. Smaller particulates, owing to their low inertia and smaller St , follow the streamlines (on which they were embedded at entry points) more closely. For larger particulates, inertia-dominated dynamics, combined with gravitational impaction, tend to inhibit downwind penetration by biasing their motion toward deposition on the walls (see panels g and especially h, in Fig 6). However, some sufficiently large particles, such as those with diameters of 10 and 15 μm (see Fig 6c-d), can still effectively maneuver around the vortex

TABLE II. Magnitude of viral load transmission into bronchial pathways as a function of inhaled particulate sizes: The duration in consideration is 3 days, with a conservative estimate of 1 particulate of each test size generated during each breathing cycle. The breathing cycles last 5 s [60].

Separated particulate size (d , in μm)	Number of virions ferried to the bronchial pathways (L_v)
15	394
10	167
5	24
1	0

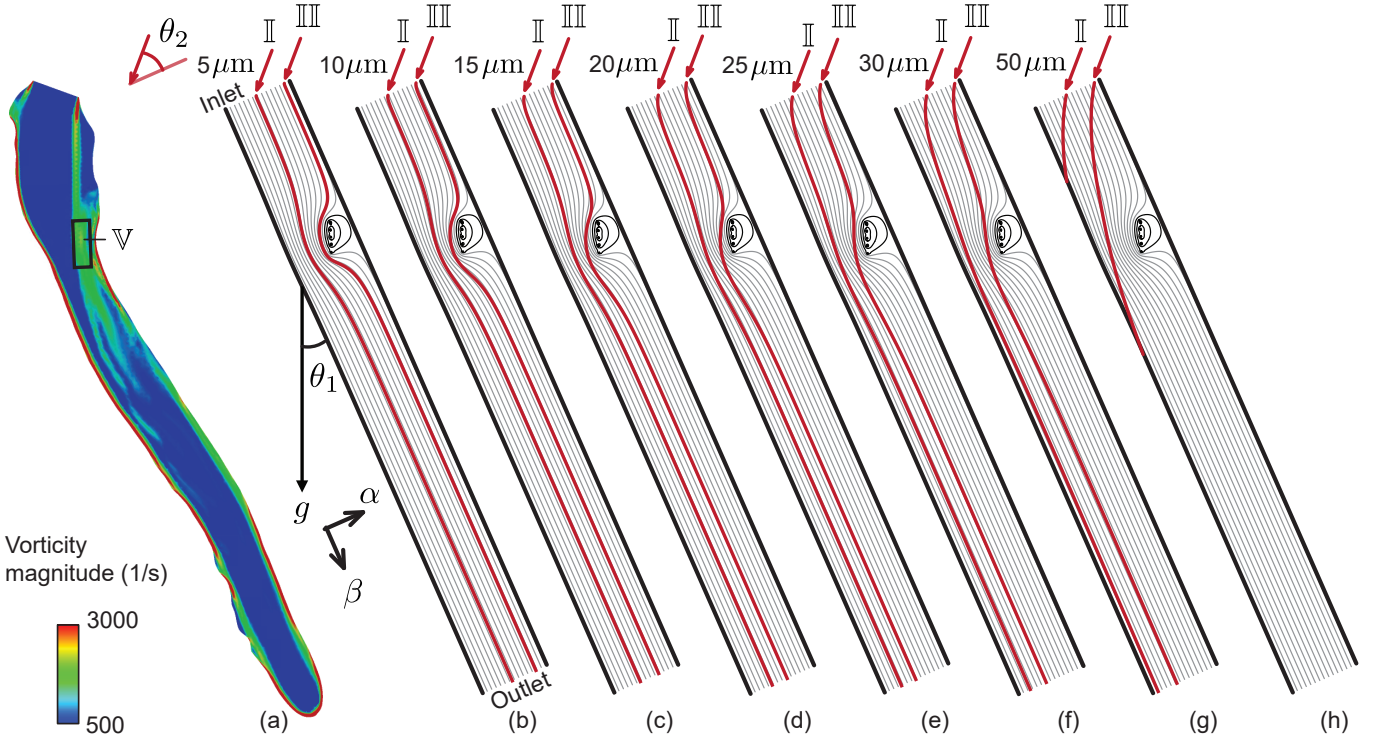


FIG. 6. **Simulation-guided analytical modeling in the laryngotracheal space.** (a) Simulated vorticity contour map on a representative two-dimensional cross-section (the S-ROAM domain) running approximately midway through the cavity; see Fig 4b. The core of the dominant vortex patch is conservatively bounded in the rectangle, marked by ∇ , with its area equating the vortex patch area A used in the S-ROAM. Panels (b-h) show two sample particle pathlines (in red) against the S-ROAM streamlines (in grey), respectively for particle sizes 5, 10, 15, 20, 25, 30, and 50 μm . The black lines on either side of the S-ROAM domain mark the slip wall boundaries. In each case, the vortex patch ∇ is mimicked by a set of five point vortices embedded on the two-dimensional flow field with background unidirectional flow in the β -direction. The representative particles entering near the middle of the inlet face and near the right edge of the model channel are respectively marked as II and III.

trap to reach the lower airspace. This trend aligns with the full-scale numerical projections.

Note that the particulates entering through the middle of the inlet face of the S-ROAM are marked as II while those entering near the right edge are marked as III. As shown in Fig 7, the particulates III, being nearer to the vortex region, are deviated more (from the airflow streamlines they were embedded on at the channel inlet) compared to the particulates II. The deviation generically grows as the particulate diameters are increased, which aligns with the numerical findings reported in Table I. A greater deviation implies that the particulates are being increasingly shifted toward the channel walls, which in turn would result in declining deposition and penetration levels in the downwind lower airway.

IV. DISCUSSION: PERSPECTIVES ON ENHANCING THE BIOPHYSICAL REALISM OF THE MODELING APPROACH

A. On the interfacial mechanics at mucociliary layers during inhalation

While the numerical and analytical models presented here conclude that particulates of the length scale $\mathcal{O}(10^1)$ μm , formed through shearing and disintegration of intra-URT mucosal filaments, can indeed have significant deposition and penetration along the bronchial tubes and in the deeper lung recesses (see Table I); to enhance the physiological realism of the model—it is essential that we obtain the actual size distribution and formation rate of the liquid particulates generated through viscoelastic separation as the inhaled air brushes past the URT mucus. The present study used the conservative estimate that 1 particulate of each size tested is formed during each breathing cycle and is a limitation.

The reader should however note that unlike expulsion regimes (during exhalation), where imaging-based data

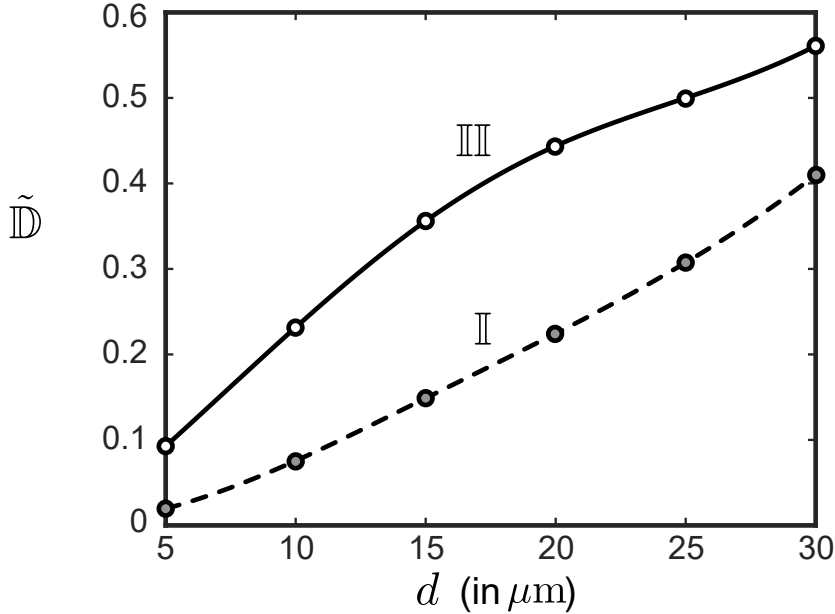


FIG. 7. **Particle transport trend in the analytical case.** Comparison of the absolute deviation (\tilde{D} , normalized with respect to the S-ROAM channel width) of the particle pathlines from the respective streamline they were embedded on at the inlet face. The deviation is measured along the α -direction (see Fig 6). Deviation curves for particles entering near the middle and the right edge of the model channel inlet are respectively marked as II and III.

collection is relatively straightforward with human subjects expelling particulates into the outside air for different speech and breathing parameters, the current problem of characterizing the internal reverse transport (inhalation) into the lower airway in live subjects could be somewhat challenging. The approach could consequently be two-fold with synergistic numerical modeling and experimental visualizations. One can consider a 2-phase interaction on anatomically realistic upper airway surfaces; the two phases being the mimicked versions of inhaled air (phase 1) and the relatively static mucosal substrate (phase 2); see Fig 8a, and explore the interfacial mechanics leading to particulate formation and release, along with their generation rate, spatiotemporal growth, and size distribution.

B. On experimental validation of deep lung penetration through in vitro physical tests

To verify the numerical modeling of the overall spatial transport, further experiments could be conducted within 3D-printed anatomically realistic airway casts internally coated with (say) concentrated glycerol (with tuned dilution levels) standing in for mucus. Controlled air flux, with embedded aerosols, could be passed through the cast via suction mechanism set up with a vacuum pump. One approach (among others) to obtain highly resolved data on lower airway penetration could be to use the sophisticated gamma scintigraphy technique [64], wherein the solution to be aerosolized and administered into the cast (with the incoming air) would be seeded with a mildly radioactive element (e.g., Technetium). After the particulates have landed along the airway walls, the radioactive signals (emitted by the deposited mass and thus presenting a measure of local penetration) could be compared with the in silico deposition patterns along the bronchial pathways. In this context, the reader may scan our previous works with experimental validations [64, 65]; in particular, [64] called on gamma scintigraphy measurements within anatomically accurate and transparent 3D-printed airway casts to physically verify numerically modeled sinonasal deposition from over-the-counter nasal sprays. The modeling protocol therein implemented similar computational schemes as in the present analysis.

C. On limitations implicit to the modeling framework and its clinical relevance

In terms of achieving true biological realism, it is important to note the limitations implicit to the numerical modeling and theoretical analysis described in this study. The approach here algorithmizes the complex dynamics of infection onset, particularly omitting the role of immune responses and mucosal properties. In an actual infection setting, the

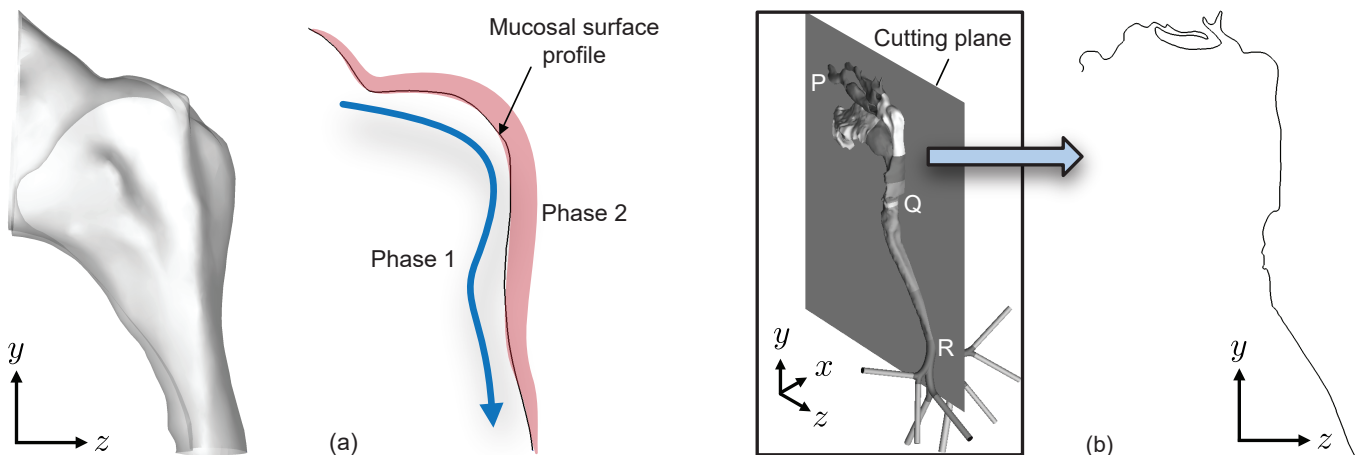


FIG. 8. **Interfacial interactions and morphological complexity along mucus-coated upper airway walls.** (a) Representative planar outline of the nasopharyngeal surface topology. Phase 1 = inhaled air; Phase 2 = mucus substrate. The blue arrow indicates the inhaled air flux sweeping over the mucus (in pale red). (b) Tortuosity measurement of the anatomical space using a sagittal cutting plane.

innate and adaptive immune responses would be activated, likely leading to dynamic alterations in mucus properties that could impact intra-URT particulate formation, clearance, and the pathogen’s state within these fragments. By focusing on a static view of mucosal fragmentation and particulate generation, this study currently does not account for such dynamic physiological responses that may influence the outcomes of viral transport and downwind deposition.

Next, the reported results, while establishing the basic plausibility of the URT-to-LRT transmission mechanism through the use of a test case, are for a specific anatomical geometry and baseline parameters that do not (yet) explicitly account for patient-to-patient variability. Realistic differences in airway anatomy, mucosal characteristics, and immune response between individuals are factors that could lead to different fragmentation and transport dynamics. Future work should incorporate sensitivity studies that test the robustness of the modeling approach across a range of physiological conditions and individual variability.

Moreover, the “so what” question remains. The findings, while *precise* in a computational sense and confirming the possibility of rapid lung invasion orchestrated by URT-derived pathogen-laden particulates, do not yet translate into actionable clinical recommendations. Future research should assess whether the insights gained could inform clinical practices or support diagnostic tools, possibly through personalized respiratory physics models that account for specific physiological traits. Such models could potentially identify subjects at higher risk of clinical morbidity, e.g., from brisk onset of severe lung infection.

V. CONCLUSION: THE MAIN TAKEAWAYS

A. Can large particulates, generated from the intra-URT mucus coating during inhalation, penetrate to the bronchial airspace?

The bronchial transmission trends from the numerical experiments (see Table I and Fig 5) are found to be consistent with the first-principles reduced-order analytical findings that modeled the impact of dominant intra-airway vortex instabilities in the laryngotracheal domain on local particle transport (Fig 6). Not only the aerosols (i.e., particulates with diameters $\lesssim 5 \mu\text{m}$) but also droplets as large as 10 and 15 μm exhibit remarkable efficiency at reaching the bronchial spaces and deep lungs, so long as they are sheared away from the URT surface and are still airborne as they enter the larynx. This contradicts the general perception that only particulates smaller than 5 μm can comfortably penetrate the lower airway. Missing the nuance therein is the fact that the incumbent perspective is based on the mechanics of particulates inhaled from the outside air, and our understanding of intra-URT mucosal breakup during inhalation and the subsequent aerial advection in the downwind tract is still nascent.

For a physics-based rationale to explain the derived deposition and penetration profiles, let us consider the tortuosity \mathcal{T} of the pathways to be traversed by a particulate inhaled from outside (called hereafter P_o), compared to a particulate that is generated within the URT and is still airborne in the laryngeal airspace (hereafter called P_u). Fig 8b illustrates a representative vertical cutting plane used to extract the tortuosity measurements. For P_o , the corresponding tortuosity is the ratio of the curved path length and the linear distance in space between the points P and R; let us represent

it as \mathcal{T}_{P_o} . For P_u , it is similarly the ratio of the curved path length and the linear distance in space between the points Q and R; let us represent it as \mathcal{T}_{P_u} . The geometric measurements return: $\mathcal{T}_{P_o} \approx 1.90$ and $\mathcal{T}_{P_u} \approx 1.04$. Consequently, if the mechanics of P_o is inertia-dominated (true for particulates $\gtrsim 5 \mu\text{m}$), they exhibit less success at navigating the highly tortuous pathway and are deposited along the anterior URT; see Fig 3 in this context. On the contrary, particulates of similar sizes, if they only have to traverse the Q-R tract, the less tortuous pathway ensures that a high percentage of them would end up reaching the bronchial domains; see Fig 5a-b. As an aside, also note that the tortuosity estimates obtained here match exactly with our previously published data on mammalian airway morphology [66]; see panel (d) in figure 1 of the cited paper. Thus, the findings of this study satisfactorily address the question Q_1 (see introduction).

B. How do the transmitted viral loads compare to the infectious dose of the test pathogen?

Infectious dose, I_D , of a virus quantifies the minimum number of virions that can potentially launch infection in an exposed subject [49, 67] and is a fundamental virological parameter. Independent studies by us [25, 26] and others [24, 68] have verified that $I_D \approx 300$, for SARS-CoV-2. Thus, evidently (per Table II), the viral load transmitted by, e.g., the 15- μm droplets would alone exceed the I_D threshold, thereby providing a mechanics-based rationale for the fast disease progression to the lower airway. The brisk pace is otherwise difficult to explain based exclusively on tissue level proliferation and direct deep lung inhalation of dominantly sub 5- μm particulates from outside. However, from a translational perspective, it is critical to note that the present *in silico* framework does not *yet* take into account the host innate and adaptive immune responses to the invading virions which can lead to shifts in mucus properties altering breakup, while affecting the dynamics of clearance and state of the virus in the URT-derived fragments. The immunological considerations, once incorporated into the mechanics paradigm, can help rationalize the varying rates of clinical prognosis recorded in different subjects [59]; e.g., deep lung infection for SARS-CoV-2 has historically ensued over a range of 2 – 8 days following the appearance of initial URT symptoms. In summary, the findings do satisfactorily address the question Q_2 posed in the introduction.

ACKNOWLEDGMENTS

The author thanks the National Science Foundation for support via the [NSF CAREER Grant, Award No. CBET 2339001](#) (Fluid Dynamics program). The author also thanks Neelesh Patankar (Northwestern University) for stimulating discussions on bronchial fluid mechanics, Julia Kimbell (School of Medicine at the University of North Carolina Chapel Hill) for providing access to existing, de-identified CT imaging, and Abby Wortman (Clinical and Lab Instructor for the Respiratory Care program at the author’s institution) for checking the nomenclature on airway physiology used in this study.

DATA SHARING

Supplemental information (including simulated data, raw files, and codes) are available on-request via OneDrive.

-
- [1] S. K. Lai, Y. Y. Wang, D. Wirtz, and J. Hanes, Micro-and macrorheology of mucus, *Advanced drug delivery reviews* **61**, 86 (2009).
 - [2] J. B. Grotberg, Respiratory fluid mechanics and transport processes, *Annual Review of Biomedical Engineering* **3**, 421 (2001).
 - [3] A. Rozhkov, Elasticity and relaxation properties of oral fluid, arXiv preprint arXiv:2112.08113 (2021).
 - [4] J. A. Moriarty and J. B. Grotberg, Flow-induced instabilities of a mucus-serous bilayer, *Journal of Fluid Mechanics* **397**, 1 (1999).
 - [5] M. Abkarian and H. A. Stone, Stretching and break-up of saliva filaments during speech: A route for pathogen aerosolization and its potential mitigation, *Physical Review Fluids* **5**, 102301 (2020).
 - [6] R. Singhal, S. Ravichandran, R. Govindarajan, and S. S. Diwan, Virus transmission by aerosol transport during short conversations, *Flow* **2** (2022).
 - [7] L. Bourouiba, The fluid dynamics of disease transmission, *Annual Review of Fluid Mechanics* **53**, 473 (2021).
 - [8] C. C. Wang, K. A. Prather, J. Sznitman, J. L. Jimenez, S. S. Lakdawala, Z. Tufekci, and L. C. Marr, Airborne transmission of respiratory viruses, *Science* **373**, eabd9149 (2021).

- [9] M. Li, Y. Saade, S. Zaleski, U. Sen, P. Kant, and D. Lohse, Viscoelasticity reduces the droplet size in mucosalivary film fragmentation during intense respiratory events, arXiv preprint arXiv:2502.05105 (2025).
- [10] X. Xie, Y. Li, H. Sun, and L. Liu, Exhaled droplets due to talking and coughing, *Journal of the Royal Society Interface* **6**, S703 (2009).
- [11] M. Lippmann and R. E. Albert, The effect of particle size on the regional deposition of inhaled aerosols in the human respiratory tract, *American Industrial Hygiene Association Journal* **30**, 257 (1969).
- [12] C. Ou, J. Hang, and Q. Deng, Particle deposition in human lung airways: effects of airflow, particle size, and mechanisms, *Aerosol and Air Quality Research* **20**, 2846 (2020).
- [13] A. Chakravarty, M. V. Panchagnula, and N. A. Patankar, Inhalation of virus-loaded droplets as a clinically plausible pathway to deep lung infection, *Frontiers in Physiology* **14**, 1073165 (2023).
- [14] W. A. N. Dorland, *Dorland's illustrated medical dictionary* (WB Saunders, 1985).
- [15] M. S. Islam, S. C. Saha, E. Sauret, T. Gemci, and Y. Gu, Pulmonary aerosol transport and deposition analysis in upper 17 generations of the human respiratory tract, *Journal of Aerosol Science* **108**, 29 (2017).
- [16] K. Inthavong, L. T. Choi, J. Tu, S. Ding, and F. Thien, Micron particle deposition in a tracheobronchial airway model under different breathing conditions, *Medical Engineering & Physics* **32**, 1198 (2010).
- [17] P. W. Longest, G. Tian, N. Khajeh-Hosseini-Dalasm, and M. Hindle, Validating whole-airway cfd predictions of dpi aerosol deposition at multiple flow rates, *Journal of Aerosol Medicine and Pulmonary Drug Delivery* **29**, 461 (2016).
- [18] M. Lazaridis, Modelling approaches to particle deposition and clearance in the human respiratory tract, *Air Quality, Atmosphere & Health* **16**, 1989 (2023).
- [19] O. S. Usmani, B. Mignot, I. Kendall, R. D. Maria, D. Cocconi, G. Georges, and N. Scichilone, Predicting lung deposition of extrafine inhaled corticosteroid-containing fixed combinations in patients with chronic obstructive pulmonary disease using functional respiratory imaging: an in silico study, *Journal of Aerosol Medicine and Pulmonary Drug Delivery* **34**, 204 (2021).
- [20] S. Verbanck, G. Ghorbaniasl, M. F. Biddiscombe, D. Dragojlovic, N. Ricks, C. Lacor, B. Ilsen, J. de Mey, D. Schuermans, S. R. Underwood, *et al.*, Inhaled aerosol distribution in human airways: a scintigraphy-guided study in a 3d printed model, *Journal of Aerosol Medicine and Pulmonary Drug Delivery* **29**, 525 (2016).
- [21] J. Schroeter, B. Asgharian, O. Price, A. Parks, D. Oldson, J. Fallica, G. Erives, C. Li, O. Rass, A. Harvanko, *et al.*, Simulation of electronic nicotine delivery systems (ends) aerosol dosimetry and nicotine pharmacokinetics, *Computational Toxicology* **31**, 100322 (2024).
- [22] W. H. Finlay, *The mechanics of inhaled pharmaceutical aerosols: an introduction* (Academic Press, 2001).
- [23] R. Wölfel, V. M. Corman, W. Guggemos, M. Seilmaier, S. Zange, M. A. Müller, D. Niemeyer, T. C. Jones, P. Vollmar, C. Rothe, M. Hoelscher, T. Bleicker, S. Brünink, J. Schneider, R. Ehmann, K. Zwirgmaier, C. Drosten, and C. Wendtner, Virological assessment of hospitalized patients with COVID-2019, *Nature* **581**, 465 (2020).
- [24] K. A. Ryan, K. R. Bewley, S. A. Fotheringham, G. S. Slack, P. Brown, Y. Hall, N. I. Wand, A. C. Marriott, B. E. Cavell, J. A. Tree, L. Allen, M. J. Aram, T. J. Bean, E. Brunt, K. R. Buttigieg, D. P. Carter, R. Cobb, N. S. Coombes, S. J. Findlay-Wilson, K. J. Godwin, K. E. Gooch, J. Gouriet, R. Halkerston, D. J. Harris, T. H. Hender, H. E. Humphries, L. Hunter, C. M. K. Ho, C. L. Kennard, S. Leung, S. Longet, D. Ngabo, K. L. Osman, J. Paterson, E. J. Penn, S. T. Pullan, E. Rayner, O. Skinner, K. Steeds, I. Taylor, T. Tipton, S. Thomas, C. Turner, R. J. Watson, N. R. Wiblin, S. Charlton, B. Hallis, J. A. Hiscox, S. Funnell, M. J. Dennis, C. J. Whittaker, M. G. Catton, J. Druce, F. J. Salguero, and M. W. Carroll, Dose-dependent response to infection with SARS-CoV-2 in the ferret model and evidence of protective immunity, *Nature Communications* **12**, 1 (2021).
- [25] S. Basu, Computational characterization of inhaled droplet transport to the nasopharynx, *Scientific Reports* **11**, 1 (2021).
- [26] S. Basu, When fluid mechanics meets virology: a modeling framework for respiratory infection onset and projection of viral infectious dose, in *APS Division of Fluid Dynamics Meeting Abstracts* (2021) pp. A01-001.
- [27] R. Mittal, R. Ni, and J. H. Seo, The flow physics of COVID-19, *Journal of Fluid Mechanics* **894** (2020).
- [28] A. Chakravarty, D. Kundu, M. V. Panchagnula, A. Mohan, and N. A. Patankar, Perspectives on physics-based one-dimensional modeling of lung physiology, arXiv preprint arXiv:2403.09203 (2024).
- [29] S. Jung, Simplified models of aerosol collision and deposition for disease transmission, *Scientific Reports* **13**, 20778 (2023).
- [30] M. Yeasin, M. M. H. Akash, and S. Basu, A mechanics-based model for inhalation-driven transmission of smallpox, in *APS Division of Fluid Dynamics Meeting Abstracts* (2024) pp. ZC05-006.
- [31] O. Erken, B. Fazla, M. Muradoglu, D. Izbassarov, F. Romano, and J. B. Grotberg, Effects of elastoviscoplastic properties of mucus on airway closure in healthy and pathological conditions, *Physical Review Fluids* **8**, 053102 (2023).
- [32] A. Chen, T. Wessler, K. Daftari, K. Hinton, R. C. Boucher, R. Pickles, R. Freeman, S. K. Lai, and M. G. Forest, Modeling insights into SARS-CoV-2 respiratory tract infections prior to immune protection, *Biophysical Journal* **121**, 1619 (2022).
- [33] C. Darquenne, A. A. T. Borojeni, M. J. Colebank, M. G. Forest, B. G. Madas, M. Tawhai, and Y. Jiang, Aerosol transport modeling: the key link between lung infections of individuals and populations, *Frontiers in Physiology* **13**, 923945 (2022).
- [34] J. M. Oakes, The utility of hybrid in silico models of airflow and aerosol dosimetry in the lung, *Journal of Biomechanics* , 112126 (2024).
- [35] S. C. Kassinos and J. Sznitman, Multiscale modeling of respiratory transport phenomena and intersubject variability, *Annual Review of Fluid Mechanics* **57** (2025).
- [36] M. J. Stephen, *Breath taking: The power, fragility, and future of our extraordinary lungs* (Atlantic Monthly Press, 2021).
- [37] J. B. West, *Respiratory Physiology: The Essentials* (Lippincott Williams & Wilkins, 2012).
- [38] S. Basu, D. O. Frank-Ito, and J. S. Kimbell, On computational fluid dynamics models for sinonasal drug transport: Relevance of nozzle subtraction and nasal vestibular dilation, *International Journal for Numerical Methods in Biomedical*

Engineering **34**, e2946 (2018).

- [39] E. L. Perkins, S. Basu, G. J. M. Garcia, R. A. Buckmire, R. N. Shah, and J. S. Kimbell, Ideal particle sizes for inhaled steroids targeting vocal granulomas: preliminary study using computational fluid dynamics, *Otolaryngology – Head and Neck Surgery* **158**, 511 (2018).
- [40] S. Basu, N. Witten, and J. S. Kimbell, Influence of localized mesh refinement on numerical simulations of post-surgical sinonasal airflow, *Journal of Aerosol Medicine and Pulmonary Drug Delivery* **30**, A (2017).
- [41] D. O. Frank-Ito, M. Wofford, J. D. Schroeter, and J. S. Kimbell, Influence of mesh density on airflow and particle deposition in sinonasal airway modeling, *Journal of Aerosol Medicine and Pulmonary Drug Delivery* **29**, 46 (2016).
- [42] D. C. Wilcox, *Turbulence modeling for CFD*, Vol. 2 (DCW industries La Canada, CA, 1998).
- [43] W. W. Kim and S. Menon, Application of the localized dynamic subgrid-scale model to turbulent wall-bounded flows, in *35th Aerospace Sciences Meeting and Exhibit* (1997) p. 210.
- [44] N. Baghernezhad and O. Abouali, Different SGS models in Large Eddy Simulation of 90° square cross-section bends, *Journal of Turbulence*, N50 (2010).
- [45] E. Ghahramani, O. Abouali, H. Emdad, and G. Ahmadi, Numerical investigation of turbulent airflow and microparticle deposition in a realistic model of human upper airway using LES, *Computers & Fluids* **157**, 43 (2017).
- [46] J. Jovanovic and I. Otic, On the constitutive relation for the reynolds stresses and the prandtl-kolmogorov hypothesis of effective viscosity in axisymmetric strained turbulence, *Journal of Fluids Engineering* **122**, 48 (2000).
- [47] G. J. M. Garcia, J. D. Schroeter, R. A. Segal, J. Stanek, G. L. Foureman, and J. S. Kimbell, Dosimetry of nasal uptake of water-soluble and reactive gases: a first study of interhuman variability, *Inhalation Toxicology* **21**, 607 (2009).
- [48] S. A. J. Morsi and A. J. Alexander, An investigation of particle trajectories in two-phase flow systems, *Journal of Fluid mechanics* **55**, 193 (1972).
- [49] V. Stadnytskyi, C. E. Bax, A. Bax, and P. Anfinrud, The airborne lifetime of small speech droplets and their potential importance in SARS-CoV-2 transmission, *Proceedings of the National Academy of Sciences* **117**, 11875 (2020).
- [50] H. Fischer, I. Polikarpov, and A. F. Craievich, Average protein density is a molecular-weight-dependent function, *Protein Science* **13**, 2825 (2004).
- [51] S. Basu, L. P. Chamorro, M. Yeasin, and M. A. Stremmer, Modeling the effect of vorticity on inhaled transport in the upper airway, arXiv preprint arXiv:2406.09708 (under review, 2024).
- [52] A. Friedmann and P. Poloubarinova, Über fortschreitende singularitäten der ebenen bewegung einer inkompressiblen flüssigkeit, *Recueil de Géophysique* **5**, 9 (1928).
- [53] H. Aref, Point vortex dynamics: a classical mathematics playground, *Journal of Mathematical Physics* **48** (2007).
- [54] S. Basu and M. A. Stremmer, Exploring the dynamics of ‘2P’ wakes with reflective symmetry using point vortices, *Journal of Fluid Mechanics* **831**, 72 (2017).
- [55] M. R. Maxey and J. J. Riley, Equation of motion for a small rigid sphere in a nonuniform flow, *Physics of Fluids* **26**, 883 (1983).
- [56] P. M. R. Maxey, Personal communication (23-June-2022).
- [57] A. Babiano, J. H. E. Cartwright, O. Piro, and A. Provenzale, Dynamics of a small neutrally buoyant sphere in a fluid and targeting in Hamiltonian systems, *Physical Review Letters* **84**, 5764 (2000).
- [58] P. Tallapragada and S. D. Ross, Particle segregation by Stokes number for small neutrally buoyant spheres in a fluid, *Physical Review E* **78**, 036308 (2008).
- [59] Y. J. Hou, K. Okuda, C. E. Edwards, D. R. Martinez, T. Asakura, K. H. Dinno III, T. Kato, R. E. Lee, B. L. Yount, T. M. Mascenik, G. Chen, K. M. Olivier, A. Ghio, L. V. Tse, S. R. Leist, L. E. Gralinski, A. Schäfer, H. Dang, R. Gilmore, S. Nakano, L. Sun, M. L. Fulcher, A. Livraghi-Butrico, N. I. Nicely, M. Cameron, C. Cameron, D. J. Kelvin, A. de Silva, D. M. Margolis, A. Markmann, L. Bartelt, R. Zumwalt, F. J. Martinez, S. P. Salvatore, A. Borczuk, P. R. Tata, V. Sontake, A. Kimple, I. Jaspers, W. K. O’Neal, S. H. Randell, R. C. Boucher, and R. S. Baric, SARS-CoV-2 Reverse Genetics Reveals a Variable Infection Gradient in the Respiratory Tract, *Cell* (2020).
- [60] RESPe, Normal breathing, [Web link](#) (accessed 23-March-2024).
- [61] K. F. Riley, M. P. Hobson, and S. J. Bence, *Mathematical methods for Physics and Engineering* (Cambridge University Press, 2004).
- [62] J. A. Nelder and R. Mead, A simplex method for function minimization, *The Computer Journal* **7**, 308 (1965).
- [63] J. C. Lagarias, J. A. Reeds, M. H. Wright, and P. E. Wright, Convergence properties of the nelder–mead simplex method in low dimensions, *SIAM Journal on Optimization* **9**, 112 (1998).
- [64] S. Basu, L. T. Holbrook, K. Kudlaty, O. Fasanmade, J. Wu, A. Burke, B. W. Langworthy, Z. Farzal, M. Mamdani, W. D. Bennett, J. P. Fine, B. A. Senior, A. M. Zanation, C. S. Ebert Jr, A. J. Kimple, B. D. Thorp, D. O. Frank-Ito, G. J. M. Garcia, and J. S. Kimbell, Numerical evaluation of spray position for improved nasal drug delivery, *Scientific Reports* **10**, 1 (2020).
- [65] M. M. H. Akash, Y. Lao, P. A. Balivada, P. Ato, N. K. Ka, A. Mituniewicz, Z. Silfen, J. D. Suman, A. Chakravarty, D. Joseph-McCarthy, and S. Basu, On a model-based approach to improve intranasal spray targeting for respiratory viral infections, *Frontiers in Drug Delivery – Sec. Respiratory Drug Delivery* **3**, [10.3389/fddev.2023.1164671](#) (This article is part of the Research Topic: Emergent Treatments for Managing Respiratory Viral Illness – Challenges and Opportunities, 2023).
- [66] J. Yuk, A. Chakraborty, S. Cheng, C. I. Chung, A. Jorgensen, S. Basu, L. P. Chamorro, and S. Jung, On the design of particle filters inspired by animal noses, *Journal of the Royal Society Interface* **19**, 1 (2022).

- [67] M. P. Zwart, L. Hemerik, J. S. Cory, J. A. G. M. de Visser, F. J. J. A. Bianchi, M. M. Van Oers, J. M. Vlak, R. F. Hoekstra, and W. Van der Werf, An experimental test of the independent action hypothesis in virus–insect pathosystems, *Proceedings of the Royal Society B: Biological Sciences* **276**, 2233 (2009).
- [68] M. Prentiss, A. Chu, and K. K. Berggren, Finding the infectious dose for COVID-19 by applying an airborne-transmission model to superspreader events, *PLOS One* **17**, e0265816 (2022).